RSC Advances

ROYAL SOCIETY OF CHEMISTRY

www.rsc.org/advances

RSC Advances

Highly Crystalline Prussian Blue/Graphene Composites for High-Rate Performance Cathodes in Na-ion Batteries

S. J. Richard Prabakar, Jaehyang Jeong and Myoungho Pyo*

Department of Printed Electronics Engineering, Sunchon National University, Sunchon, Chonnam 540-742, Republic of Korea.

E-mail: mho@sunchon.ac.kr; Fax: +82 61 750 5260; Tel: +82 61 750 3638

Abstract

We report the synthesis of highly crystalline Prussian Blue (PB) embedded in graphene oxide (GO) layers and its superior electrochemical properties. Highly crystalline PB is prepared from Fe_2O_3 nanoparticles anchored on GO (Fe_2O_3/GO). Regulated Fe^{3+}-ion release and slow crystallization with $[Fe(CN)_6]$ in the vicinity of Fe_2O_3/GO produce a GO-interconnected PB (HC-PB/GO) with fewer $[Fe(CN)_6]$ vacancies and H_2O molecules. When compared with PB synthesized under identical conditions without GO, the HC-PB/GO delivers a noticeably higher reversible capacity and better cyclability as a cathode in Na-ion batteries (SIBs). The improvement in high-rate performance is rather striking. While the energy density of PB at a charge/discharge (C/D) rate of 2.0 $A{\cdot}g^{-1}$ is negligible, the HC-PB/GO delivers 280 $mWh{\cdot}g^{-1}$. The increase of electronic conduction and Na^+ ion diffusion in HC-PB/GO contribute to a substantial improvement in rate capability.

Introduction

It is universally accepted that sustainable energy will become an essential commodity in the near future, and this phenomenon will be accompanied by the concomitant necessity of more efficient energy storage systems (ESS). Rechargeable batteries are one of the most promising means for storing energy on a large-scale, mainly because of high energy conversion efficiency and simple maintenance.[1] Despite these advantages, the extensive application of rechargeable batteries to a large-scale ESS requires the consideration of another economical aspect. Though the technology of Li ion batteries (LIBs) is now sufficiently reliable,[2-5] the fast depletion of Li resources due to extensive consumption for ESS is expected to raise production costs,[6,7] eventually making the comprehensive use of LIBs in ESS questionable. To overcome this hurdle, room temperature Na-ion batteries (SIBs) have been proposed as a suitable alternative to LIBs for large-scale ESS.[8-10] The relatively large ionic radius of Na^+ (1.02 Å for sodium vs. 0.76 Å for lithium), however, makes it impossible to use the same electrode materials as LIBs. Particularly in the case of cathodes, the slow mobility of Na^+ ions in closely packed crystalline structures causes poor rate capability.[11-14]

In this regard, Prussian blue (PB) and its analogues with an open framework could be a suitable strain-free cathode for SIBs.[15-23,] PB is a venerable coordination compound and has the following general formula: $A_xM^1[M^2(CN)_6]_y\cdot\square_{1-y}\cdot nH_2O$ ($0 < x < 2$; $y < 1$); where A signifies alkaline metal ions, M^1 and M^2 represent transition metal ions, and $\square$ denotes the $[M^2(CN)_6]$ vacancy occupied by coordinating water. The face-centered cubic structure of PB (space group symmetry *Fm*-3*m*) consists of cyano-bridged M_1 and M_2 ions residing in an alternate sequence,

and it possesses relatively large interstitial voids that allow the accommodation of most alkaline metal cations without undergoing severe structural deformations during the reduction of M_1 and M_2. By virtue of these structural features, PB and its analogues are also regarded as promising cathode materials in aqueous rechargeable batteries that use a variety of large monovalent cations.[24-27]

When synthesized by the conventional route, however, PB includes substantial vacancies and zeolitic water in its crystalline structure.[28] The presence of $[Fe(CN)_6]$ vacancies and the water molecules (coordinated to Fe^{3+} and/or uncoordinated (zeolitic) within interstitial voids) decreases the amount of inserted/de-inserted Na^+ ions, and also aggravates the structural stability during repeated charge/discharge (C/D) cycles in SIBs. In addition, a collapse of $–Fe^{2+}$-$(CN)_6$-Fe^{3+}-bridges and an occlusion of zeolitic water result in a decrease in the electronic conduction through the PB framework and a decrease in the Na^+ mobility, respectively, which lowers the rate performance of SIBs. Hence, the preparation of highly crystalline PB with low defect sites and low H_2O content is essential in assuring its viability in SIBs. Y. You et al and Y. Liu et al. recently reported the use of a high quality PB crystal as a cathode in SIBs.[18,21] High quality PB, $Na_{0.61}Fe[Fe(CN)_6]_{0.94}\cdot\square_{0.06}$, showed a stable cyclic response, and delivered high reversible capacities (over 160 $mAh\cdot g^{-1}$) that was superior to low quality PB at a rate of 25 $mA\cdot g^{-1}$. Nonetheless, its reversible capacity was significantly decreased to less than 60 $mAh\cdot g^{-1}$ at 600 $mA\cdot g^{-1}$, requiring further improvements in rate performance in order to obtain a high degree of practicality.

In the present work, we describe the synthesis of a highly crystalline PB composited with graphene oxide (HC-PB/GO). The controlled release of Fe^{3+} from Fe_2O_3 nanoparticles which are evenly anchored on and densely packed with GO (Fe_2O_3/GO) facilitates the formation of HC-PB on GO via slow crystallization kinetics (Scheme 1). The formation of PB via the decomposition of $[Fe(CN)_6]$ in a solution is minimized. HC-PB/GO possesses low $[Fe(CN)_6]$ vacancies, which leads to excellent rate performance when applied as a cathode in SIBs. The reduced structural and compositional imperfection in PB and the well-interconnected graphene layers in HC-PB/GO contribute to a superior rate capability.

Experimental

1. Synthesis of Fe_2O_3/GO

All chemicals used were purchased from Aldrich, unless otherwise mentioned. GO was synthesized via a modified Hummer's method.[29] For the synthesis of Fe_2O_3/GO, GO (200 mg) was dispersed in deionized water (60 mL). Then, acetic acid (10.5 mL) was added and stirred, followed by the addition of $FeCl_3 \cdot 6H_2O$ (0.96 g). The solution was mixed vigorously until the $FeCl_3$ was fully dissolved and the GO was homogenously dispersed. The reaction mixture was transferred into a Teflon-lined autoclave, following the addition of an ammonia solution (10.5 mL, 30 wt%). The Fe_2O_3 formation reaction proceeded at 160 ^oC for 48 h. The product was collected by centrifuge, washed with deionized water and ethanol, and dried at 80 ^oC overnight. Fe_2O_3 nanoparticles (NPs) were synthesized by a similar procedure without the addition of GO.

2. Synthesis of HC-PB/GO

For the synthesis of HC-PB/GO, 100 mg of Fe_2O_3/GO (ca. 72 mg of Fe_2O_3, see Fig. 1C) was dispersed in deionized water (39 mL) using a bath sonicator. $Na_4[Fe(CN)_6]$ (96.8 mg, 0.2 mmole) in deionized water (39 mL) was added to the Fe_2O_3/GO solution and stirred vigorously for 10 min. HCl (37 wt%, 2.0 mL) was then added to attain ca. 1 wt% HCl. The mixture was stirred in a round bottom flask at 60 ^oC for 4 days with constant N_2 bubbling. The solution color turned to pale blue after 30 min and gradually deepened with reaction time. The product was separated by centrifuge and washed with deionized water and ethanol. The composite was dried in vacuum at 100 ^oC for 2h. The final products were transferred immediately into airtight vials and stored under ambient conditions. For comparison, PB was also synthesized from Fe_2O_3 NPs without GO.

3. Characterization

The compositions of PB in HC-PB/GO were determined using elemental analysis (Leco TrueSpec) and inductively coupled plasma atomic emission spectroscopy (ICP-AES, Varian 720ES). The relative weight fraction of GO was confirmed by thermogravimetric analysis (TGA, TA Instruments Q50). X-ray diffraction (XRD) patterns were recorded using a Rigaku ULTIMA 4 equipped with Cu Kα radiation at a scan rate of $5°\cdot min^{-1}$. Field emission scanning electron microscope (FESEM) investigations were carried out using a JEOL JSM-7100F. High-resolution transmission electron microscope (HRTEM) images were obtained using a TEM JEOL 2100 instrument with an accelerating voltage of 200 kV. The coin cells (CR 2032) had a Na/electrolyte/HC-PB/GO (or PB) configuration, wherein the separator was sandwiched

between two electrodes, and were assembled in an Ar-filled glove box (O_2, H_2O < 1 ppm). The cathode electrode was a mixture of 80% HC-PB/GO (or PB), 10% poly(vinylidene fluoride), and 10% acetylene black (MTI, USA). The slurry was coated on Cu foil and punched into the required size after drying and roll-pressing (film thickness = ca. 10 μm, active mass = ca. 0.0023 g). The electrolyte was 1.0 M $NaClO_4$ dissolved in a mixed solvent of equal volumes of ethylene carbonate (EC) and diethyl carbonate (DEC). Galvanostatic C/D cycle tests were performed using an automatic WBCS 3000 battery cycler (WonATech) in a potential range of 2.0-4.2 V vs. Na/Na^+. Electrochemical impedance spectroscopy (EIS) was performed by applying a sine wave with an amplitude of 10.0 mV for frequencies ranging from 100 KHz to 0.1 Hz. The extraction of electrochemical parameters was performed using Zview software.

Results and discussion

The X-ray diffraction (XRD) patterns for Fe_2O_3/GO and Fe_2O_3 NPs are shown in Fig. 1A. The diffraction patterns of Fe_2O_3 NPs coincided with that of Fe_2O_3/GO, indicating a hematite α-Fe_2O_3 structure with an R-3c space group (JCPDS # 024-0072), regardless of the presence of GO. The diffraction peak that resulted from the long-range order of the graphene layers (2θ of ca. 24^o) was absent in Fe_2O_3/GO. This suggested that, although GO was believed to be partially reduced during Fe_2O_3/GO synthesis (The color of the reaction mixture was changed from brown to black with time.), the restacking of graphene layers into graphitic domains was minimized. The composite contained ca. 72 wt% of Fe_2O_3, as evidenced by TGA of the Fe_2O_3/GO in air (Fig. 1B). Although the graphene layers were not stacked in an orderly manner, the microscopic image of Fe_2O_3/GO showed a densely packed structure with Fe_2O_3 NPs homogeneously

distributed and anchored on GO layers (Fig. 1C). A magnified view of the FESEM image clearly reveals these features. All Fe_2O_3 NPs with an average particle size of ca. 75 nm and no serious aggregates were in contact with GO layers. The TEM images of the Fe_2O_3/GO composite confirm the particle size (Fig. S1 in the Supplementary Information) of Fe_2O_3 in the Fe_2O_3/GO composite. Closer inspections of the Fe_2O_3 nanoparticles (Inset of Fig. S1 in the Supplementary Information) reveal a "flower like" structure containing agglomerated nanoparticles of size ~20 nm.

In order to prepare highly crystalline PB on GO, the series of samples were synthesized under different reaction temperatures and atmospheric conditions. The composites were synthesized in 1.0 wt% HCl under air at low (0 ^{o}C), room (25 ^{o}C), and high (60 ^{o}C) temperatures as well as under N_2 at 60 ^{o}C. The XRD patterns of the composites shown in Fig. 2 were well indexed to a face-centered cubic structure (space group *Fm*3*m*), but the PB synthesized under air at low (pattern a) and room (pattern b) temperatures showed remnant Fe_2O_3 impurities. The impurities were not eliminated by extending the reaction time, which suggested that they were not due to slow reaction kinetics (i.e., slow Fe^{3+} dissolution) at these temperatures. An increase in the reaction temperature to 60 ^{o}C, on the other hand, seemed to significantly shift the equilibrium state to the product. The diffraction intensities (Fig. 2C) became quite intense, and the impurity peaks disappeared. The PB was also synthesized on GO under N_2 at 60 ^{o}C. The XRD pattern (Fig. 2d) was identical to Fig. 2C, but showed slightly more intense peaks. The 2θ position of (200) reflection was also shifted from 17.36 to 17.40^{o} after changing the atmosphere which corresponded to a slight decrease in lattice parameter 'a' from 10.21 to 10.18 Å. The constant N_2 purge seemed to help the formation of a highly crystalline PB, because the aerial oxidation of Fe^{2+} ions, which was formed by the acidic decomposition of $Na_4[Fe(CN)_6]$,

was suppressed. Therefore, the maintenance of an inert atmosphere was believed to be crucial for the PB preparation of high crystallinity by limiting the Fe^{3+} source to Fe_2O_3 (Hereafter, HC-PB/GO denotes the composite synthesized under N_2 at 60 ^{o}C.).

The compositions of PB and HC-PB/GO were confirmed via a combination of elemental analysis and inductively coupled plasma atomic emission spectroscopy (ICP-AES). For the determination of a PB formula in HC-PB/GO, the GO was assumed to have a completely reduced structure (i.e., no oxygen content). This could cause an error wherein the H_2O content in the HC-PB/GO could be over-estimated. Considering that non-stoichiometrically excessive 'C' relative to 'N' was due to the GO in PC-PB/GO, the formula of the PB was determined to be $Na_{0.72}Fe[Fe(CN)_6]_{0.90}\cdot\square_{0.10}\cdot 1.0H_2O$, which indicated relatively small vacancies. This was contrasted with the substantial vacancies and high H_2O content of the PB that had been synthesized with no GO, $Na_{0.26}Fe[Fe(CN)_6]_{0.72}\cdot\square_{0.28}\cdot 2.1H_2O$. Despite the over-estimation, therefore, the results clearly revealed that the H_2O content in HC-PB/GO was significantly less than that in the PB alone. The substantially reduced $[Fe(CN)_6]$ vacancies and H_2O content in HC-PB/GO implied that the use of Fe_2O_3/GO as a precursor was important in preparing a near-perfect PB structure.

The reduced H_2O content in HC-PB/GO was also confirmed by examining its thermal stability. The TGA profiles of PB and HC-PB/GO, which were measured in air, are shown in Fig. 3. In general, the TGA profile of PB was known to be complex, experiencing several decomposition processes.[18,30] The HC-PB/GO also showed corresponding behaviors. The weight loss below 250 ^{o}C, which resulted from coordinated H_2O molecules and occluded zeolytic water, were ca. 12.0 and 6.5 wt% in PB and HC-PB/GO, respectively. (Based on the formulas, the values for the

content of H_2O were 15.0 and 6.4 wt% for PB and HC-PB/GO, respectively.). Another distinctive difference in TGA profiles between PB and HC-PB/GO was also observed at a temperature range of 360 ~ 460 ^oC. The invariance of weight at this temperature range in PB suggested that the ca. 18 % weight-loss in HC-PB/GO could be attributed to the decomposition of the graphene layers. Since the negligible residue of GO remained at higher than 600 ^oC in air,[4] the fraction of GO in the HC-PB/GO was considered equal to 18 wt%.

The use of Fe_2O_3/GO in preparing HC-PB/GO also affected the size of the PB crystals and the degree of defect formation. A comparison of FESEM images of PB and HC-PB/GO (Fig. 4) revealed that, while the PB in HC-PB/GO had well-developed cube shapes with sizes ranging from 300~500 nm, the PB synthesized without GO had smaller-sized cubes (100~200 nm) with substantial holes and craters. Fig 4B also shows that the GO layers were in close contact with the PB cubes, implying the additional role of GO for electronic conduction between the cubes. The controlled release of Fe^{3+} from Fe_2O_3/GO and the slow crystallization of PB on the surface of GO were believed to result in PB that was smaller and defect-free. The homogeneous distribution of PB cubes with GO was also confirmed by TEM images (Fig. 5A and 5B). It was evident that the well-crystallized PB cubes were tightly interconnected by the corrugated GO layers. The PB crystal showed a perfect cubic shape with no defects or imperfections. The selected area diffraction pattern (SAED) captured on a single PB particle along the [001] zone axis (Fig. 5C) displayed cubic symmetry diffraction spots, which indicated the single crystal nature of the cubes.

Expecting improved electrochemical properties, based on its high crystallinity and reduced H_2O content, the performance of HC-PB/GO as a cathode in SIBs was examined. The

C/D profiles of PB and HC-PB/GO are shown in Fig. 6A and 6B. The two plateaus located at ca. 3.0 and 3.4 V were evident for both materials and were related to the redox reactions of low and high spin Fe^{2+}/Fe^{3+} redox, respectively. Although both the electrodes showed similar profiles, the reversible capacity of HC-PB/GO was noticeably greater than that of PB alone. HC-PB/GO showed a ca. 30 % higher capacity than that of PB alone during the 1st discharge (113 vs. 87 mAh·g^{-1}). The increased discharge capacity during the 2nd cycle due to the activation of a low spin Fe^{2+}/Fe^{3+} redox process did not alter the ratio (150 vs. 115 mAh·g^{-1}). With repeated cycling, however, the differences in reversible capacities became gradually more conspicuous, indicating the better cyclability of HC-PB/GO (Fig. 6C). While the capacity of PB was quickly depleted with a fading rate of 0.44 mAh·g^{-1}·cycle^{-1}, the capacity of 150 mAh·g^{-1} in HC-PB/GO during the 2nd cycle showed a slight decay with a fading rate of 0.27 mAh·g^{-1}·cycle^{-1}. The Coulombic efficiencies of HC-PB/GO were also slightly higher throughout, displaying 80.6 and 74.9 % during the 1st C/D cycle for HC-PB/GO and PB, respectively. The higher reversible capacity and the better cyclability of HC-PB/GO could be a direct consequence of fewer vacancies and a lower H_2O content. Cyclic voltammetry studies were carried out to validate the enhanced reversibility of HC-PB/GO. The CV for both electrodes in 1.0 M $NaClO_4$ at a scan rate of 0.1 mV·s^{-1} vs Na/Na^+ is shown in Fig. S2 (in the Supplementary Information). The CV for PB (curve a) shows two definite pairs of nearly symmetric and reproducible redox peaks located at a formal potential ($(E_{pa} + E_{pc})/2 = E_{1/2}$) of 3.43 and 2.92 V, respectively. In case of HC-PB/GO (curve b), the two peaks appeared at an $E_{1/2}$ of 3.50 and 2.96 V, respectively. The peak separation for the peak located at the higher voltage of 3.50 V (responsible for the majority of

Na^+ storage) for HC-PB/GO was 0.204 V, in contrast to 0.316 V for PB. This noticeable difference in the peak separation implies a highly reversible redox reaction facilitated in HC-PB/GO.

The presence of vacancies can hamper the electron transport along the C≡N framework, increasing the polarization. In addition, the large amount of zeolitic water in a framework competes with Na^+ ion diffusion, decreasing Na^+ mobility.[18] The highly crystalline nature of PB in HC-PB/GO, therefore, can be expected to improve the rate performance when used as a cathode in SIBs. Furthermore, since GO layers tightly interconnect the PB cubes, a more facile degree of electronic conduction is also expected. The stepwise rate performance examination between 25 and 500 $mA \cdot g^{-1}$ is shown in Fig. 7A. As expected, while the capacity of PB dropped from 115 $mAh \cdot g^{-1}$ at 25 $mA \cdot g^{-1}$ to 86 $mAh \cdot g^{-1}$ at 500 $mA \cdot g^{-1}$, the capacity of HC-PB/GO was decreased by only 15 $mAh \cdot g^{-1}$ (150 $mAh \cdot g^{-1}$ at 25 $mA \cdot g^{-1}$ and 135 $mAh \cdot g^{-1}$ at 500 $mA \cdot g^{-1}$). The superiority of the rate performance became pronounced with increases in the C/D rates. After returning the rate to 25 $mA \cdot g^{-1}$, the capacities were immediately recovered to the initial levels for both materials (Recovery to the identical value was impossible due to fading.).

The rate performance was further investigated by increasing the current densities until the capacity reached a complete depletion (Fig. 7B and 7C). PB showed a substantial decrease in the capacity with increases in the current densities. In particular, the profile was severely distorted, and the capacity became negligible when the current density was greater than 500 $mA \cdot g^{-1}$. In contrast, HC-PB/GO showed significant capacities, even at more than 500 $mA \cdot g^{-1}$. HC-PB/GO delivered capacities of 122 and 107 $mAh \cdot g^{-1}$ at 1,000 and 2,000 $mA \cdot g^{-1}$, respectively. To demonstrate the superior rate performance of HC-PB/GO, at high rates in particular, the energy and power densities were compared with those of PB. A Ragone plot clearly indicated that HC-

PB/GO delivered significantly higher energy and power densities than PB (Fig. 7D). For instance, HC-PB/GO showed an energy density of 338 $Wh \cdot kg^{-1}$ and a power density of 2,800 $W \cdot kg^{-1}$ at 1,000 $mA \cdot g^{-1}$, in contrast with 123 $Wh \cdot kg^{-1}$ and 2,515 $W \cdot kg^{-1}$ for PB, respectively, indicating that HC-PB/GO is a promising candidate for applications as a high-rate cathode in SIBs.

To further elucidate the kinetics of the electrode reaction, EIS studies were performed. The Nyquist plots of PB and HC-PB/GO were obtained for as-prepared, 1-cycled, and 5-cycled cells (Fig. 8). The Nyquist plot showed a depressed semi-circle in the high frequency region, which was attributed to the charge-transfer phenomenon, and a linear sloping region in the low frequency range, which was related to the semi-infinite Warburg diffusion process. Before cycling, both electrodes showed identical curves with charge-transfer resistances (R_{ct}) of 371.2 and 359.7 Ω for PB and HC-PB/GO, respectively. The similarity of the Nyquist plots, however, was not held after C/D cycling. The large drop of the R_{ct} from 359.7 to 79.5 Ω in HC-PB/GO was in contrast to the small decrease in PB (from 371.2 to 276.1 Ω). The R_{ct} of HC-PB/GO remained almost invariant after five C/D cycles, indicating that the electrochemical reaction reached a steady-state. On the other hand, a slight increase in R_{ct} (from 276.1 to 303.6 Ω) was observed for PB during five C/D cycles. These observations implied that the higher electronic conductivity in HC-PB/GO, due to fewer vacancies and interconnecting GO layers, led to a smaller R_{ct} and eventually provided the composite with excellent high-rate characteristics.

The effect of less water content in HC-PB/GO on Na^+ ion diffusion was also examined. The apparent diffusion coefficient (D_{Na}) was calculated from the inclined line in the Warburg region (Fig. 8A), using the following equation:

$$D = R^2T^2 / 2A^2n^4F^4C^2\sigma^2$$

where R is the gas constant, T is the absolute temperature, A is the surface area of the cathode electrode, n is the number of electrons per molecule during oxidation, F is the Faraday constant, C is the Na^+ concentration, and σ is the Warburg factor associated with Z_{re}. The value for σ was obtained from the linear fitting of Z_{re} with respect to the reciprocal square root of the angular frequency. D_{Na} values of 5.11 x 10^{-13} and 9.80 x 10^{-13} $cm^2 \cdot s^{-1}$ were obtained for PB and HC-PB/GO, respectively. Although small, the noticeable difference in the diffusion kinetics was ascribed to a lower water content in HC-PB/GO, which promoted increases in the rate of Na^+ ion diffusion. It is also worth noting that, after five C/D cycles, the Nyquist curve of PB displayed a new semi-circle in the high frequency region (denoted by 39.8 kHz in Fig. 8C), which was not evident in HC-PB/GO. This allowed us to speculate that the graphene layers in HC-PB/GO might have suppressed the formation of a thicker surface-electrolyte-interface (SEI) layer.[31-33] The reduced surface area of the PB that was in contact with electrolytes, due to being densely packed within the GO stacks, was believed to have contributed to the suppression of excessive SEI layer formation.

Since the high crystallinity of the PB in HC-PB/GO can ensure the maintenance of the structural features after repeated C/D cycling, the morphology changes of HC-PB/GO, which was subjected to 100 C/D cycles at 25 $mA \cdot g^{-1}$, were examined by FESEM (Fig. 9). The FESEM image of the HC-PB/GO electrode (washed with dry acetonitrile to remove the binder) indicated that the cubic morphology of the PB had not deteriorated and no new defects (holes and craters shown for as-prepared PB in Fig. 4) had formed during the C/D cycling. However, the PB seemed to have experienced severe pulverization, which resulted in smaller blunt particles. The

cubic morphology was difficult to discern. The structural integrity of PB seemed to be assured in GO-interconnected PB, which possessed fewer vacancies and fewer water molecules.

Conclusions

In summary, we have synthesized highly crystalline PB by using Fe_2O_3-anchored GO. The slow crystallization rate of PB, resulting from the presence of GO and from an inert atmosphere, produced PB with fewer $[Fe(CN)_6]$ vacancies and fewer water molecules. PB cubes were also interconnected by tightly bound GO, conferring an electronic conduction pathway in HC-PB/GO. From the combination of these characteristics, HC-PB/GO showed higher reversible capacities and better cyclability, when compared with PB synthesized without GO. The most striking features of HC-PB/GO, however, were found in its high-rate performance. The continuous decrease of capacities in PB with current densities, delivering only an energy density of 46 $mWh \cdot g^{-1}$ at 2000 $mA \cdot g^{-1}$, was not the case in HC-PB/GO. A significantly higher energy density (280 $mWh \cdot g^{-1}$) was obtained at the same current density in HC-PB/GO. The energy density of HC-PB/GO was not depleted even at 5,000 $mA \cdot g^{-1}$, delivering 192 $mWh \cdot g^{-1}$. The excellent energy densities at high rates were associated with the high degrees of electronic and Na^+ ionic conduction, which resulted from the near-perfect structures of PB and the tightly bound PB cubes by the GO layers. This new method utilizing precursor-anchored GO (i.e., Fe_2O_3/GO in this study) represents a new platform for synthesizing other graphene-supported cathode materials in SIBs.

Acknowledgements

This research was supported by Basic Science Research Program through the National Research Foundation of Korea (NRF) funded by the Ministry of Education (NRF-2014R1A6A1030419).

Scheme & Figure captions

Scheme 1 Schematized view of the controlled release of Fe^{3+} from Fe_2O_3/GO and the formation of HC-PB on GO via slow crystallization kinetics.

Figure 1 (A) XRD patterns of Fe_2O_3 NPs and Fe_2O_3/GO composite. (B) TGA profile of Fe_2O_3/GO measured at a heating rate of 10 $^{o}C \cdot min^{-1}$ in air. (C) FESEM image of Fe_2O_3/GO and a magnified view (right).

Figure 2 XRD patterns of the composites synthesized at (a) 0, (b) 25, and (c) 60 ^{o}C. (d) XRD pattern of HC-PB/GO synthesized at 60 ^{o}C with constant N_2 bubbling.

Figure 3 TGA profile of PB and HC-PB/GO measured at a heating rate of 10 $^{o}C \cdot min^{-1}$ in air.

Figure 4 FESEM images of (A) PB and (B) HC-PB/GO.

Figure 5 TEM images of HC-PB/GO at (A) low and (B) high magnification. (C) SAED pattern taken from a single PB particle along the [001] zone axis.

Figure 6 C/D curves of the 1st, 2nd and 10th cycles for (A) PB and (B) HC-PB/GO at 25 $mA \cdot g^{-1}$. (C) Capacity retention of PB and HC-PB/GO at a rate of 25 $mA \cdot g^{-1}$.

Figure 7 (A) Rate capability of PB and HC-PB/GO with stepwise increases of C/D rates from 25 to 500 $mA \cdot g^{-1}$ and a return to 25 $mA \cdot g^{-1}$. Numbers indicate the current density in $mA \cdot g^{-1}$. (B) Discharge profiles of PB at current densities of 0.025, 0.05, 0.1, 0.2, 0.3, 0.5, 1.0, and 2.0 $A \cdot g^{-1}$. (C) Discharge profiles of HC-PB/GO at current densities of 0.025, 0.05, 0.1, 0.2, 0.3, 0.5, 1.0, 2.0, 3.0, and 5.0 $A \cdot g^{-1}$. (D) Ragone plot of PB and HC-PB/GO.

Figure 8 EIS spectra for PB and HC-PB/GO electrodes. (A) As-assembled cells at open circuit potential and (B) one- and (C) five-cycled cells in a fully charged state.

Figure 9 FE-SEM images of (A) PB and (B) HC-PB/GO after 100 C/D cycles at a rate of 25 $mA \cdot g^{-1}$. The cathode electrode was sonicated gently in dry acetonitrile several times to remove the binder, then dried before analysis.

Notes and references

[1] B. Dunn, H. Kamath and J.-M. Tarascon, *Science*, 2011, **334**, 928-935.

[2] A. Kraytsberg and Y. Ein-Eli, *Adv. Energy Mater.,* 2012, **2**, 922-939.

[3] S. J. Richard Prabakar, Y.-H. Hwang, E.-G. Bae, S. Shim, D. Kim, M. S. Lah, K.-S. Sohn and M. Pyo, *Adv. Mater*. 2013, **25**, 3307-3312.

[4] Y.-H. Hwang, E. G. Bae, K.-S. Sohn, S. Shim, X. Song, M. S. Lah and M. Pyo, *J. Power Sources,* 2013, **240**, 683-690.

[5] B. Lee, S. C. Han, M. Oh, M. S. Lah, K.-S. Sohn and M. Pyo, *Electrochim. Acta.*, 2013, **113**, 149-155.

[6] "Lithium" in Mineral Commodity Summaries 2012 , U. S. Geological Survey, Reston, VA, 2012 , p. 94.

[7] J.-M. Tarascon, *Nat. Chem*., 2010, **2**, 510.

[8] M. D. Slater, D. Kim, E. Lee and C. S. Johnson, *Adv. Funct. Mater*., 2013, **23**, 947-958.

[9] S. P. Ong, V. L. Chevrier, G. Hautier, A. Jain, C. Moore, S. Kim, X. Ma and G. Ceder, *Energy Environ. Sci.*, 2011, **4**, 3680-3688.

[10] H. Pan, Y.-S. Hu and L. Chen, *Energy Environ. Sci*., 2013, **6**, 2338-2360.

[11] S. C. Han, H. Lim, J. Jeong, D. Ahn, W. B. Park, K.-S. Sohn and M. Pyo, *J. Power Sources*, 2015, **277**, 9-16.

[12] S. Komaba, C. Takei, T. Nakayama, A. Ogata and N. Yabuuchi, *Electrochem. Commun.,* 2010, **12**, 355-358.

[13] A. Langrock, Y. Xu, Y. Liu, S. Ehrman, A. Manivannan and C. Wang, *J. Power Sources,* 2013, **223**, 62-67.

[14] J. Zhao, J. Xu, D. H. Lee, N. Dimov, Y. S. Meng and S. Okada, *J. Power Sources,* 2014, **264**, 235-239.

[15] Y. H. Lu, L. Wang, J. G. Cheng and J. B. Goodenough, *Chem. Commun*., 2012, **48**, 6544-6546.

[16] L. Wang, Y. Lu, J. Liu, M. Xu, J. Cheng, D. Zhang and J. B. Goodenough, *Angew. Chem. Int. Ed.,* 2013, **52**, 1964-1967.

[17] X. Wu, W. Deng, J. Qian, Y. Cao, X. Ai and H. Yang, *J. Mater. Chem. A*, 2013, **1**, 10130-10134.

[18] Y. You, X.-L. Wu, Y.-X. Yin and Y.-G. Guo, *Energy Environ. Sci.,* 2014, **7**, 1643-1647.

[19] T. Matsuda, M. Takachi and Y. Moritomo, *Chem. Commun*., 2013, **49**, 2750-2752.

[20] S.-H. Yu, M. Shokouhimehr, T. Hyeon and Y.-E. Sung, *ECS Electrochem. Lett*., 2013, **2**, A39-A41.

[21] Y. Liu, Y. Qiao, W. Zhang, Z. Li, X. Ji, L. Miao, L. Yuan, X. Hu and Y. Huang, *Nano Energy*, 2015, **12**, 386-393.

[22] W.-J. Li, S.-L. Chou, J.-Z. Wang, J.-L. Wang, Q.-F. Gu, H.-K. Liu and S.-X. Dou, *Nano Energy,* 2015, **13**, 200-207.

[23] D. Yang, J. Xu, X.-Z. Liao, Y.-S. He, H. Liu and Z.-F. Ma, *Chem. Commun*., 2014, **50**, 13377-13380.

[24] M. Pasta, C. D. Wessells, N. Liu, J. Nelson, M. T. McDowell, R. A. Huggins, M. F. Toney and Y. Cui, *Nat. Commun.,* 2014, **5**, 30071-30079.

[25] R. A. Huggins, *J. Electrochem. Soc*., 2013, **160**, A3020-A3025.

[26] C. D. Wessells, M. T. McDowell, S. V. Peddada, M. Pasta, R. A. Huggins and Y. Cui, *ACS Nano*, 2012, **6**, 1688-1694.

[27] C. D. Wessells, S. V. Peddada, R. A. Huggins and Y. Cui, *Nano Lett*., 2011, **11**, 5421-5425.

[28] P. R. Bueno, D. Gimnnez-Romero, C. Gabrielli, J. J. Garcia-Janeno, H. Perrot and F. Vicente, *J. Am. Chem. Soc.*, 2006, **128**, 17146-17152.

[29] S. J. Richard Prabakar, R. S. Babu, M. Oh, M. S. Lah, S. C. Han, J. Jeong and M. Pyo, *J. Power Sources*, 2014, **272**, 1037-1045.

[30] A. M. Farah, C. Billing, C. W. Dikio, A. N. Dibofori-Orji, O. O. Oyedeji, D. Wankasi, F. M. Mtunzi and E. D. Dikio, *Int. J. Electrochem. Sci*., 2013, **8**, 12132-12146.

[31] S. J. Richard Prabakar, Y.-H. Hwang, B. Lee, K.-S. Sohn and M. Pyo, *J. Electrochem. Soc.*, 2013, **160**, A832-A837.

[32] S. P. Kim, A. C. T. van Duin and V. B. Shenoy, *J. Power Sources*, 2011, **196**, 8590-8597.

[33] S. J. Richard Prabakar, Y.-H. Hwang, E. G. Bae, D. K. Lee and M. Pyo, *Carbon*, 2013, **52**, 128-136.

Scheme 1

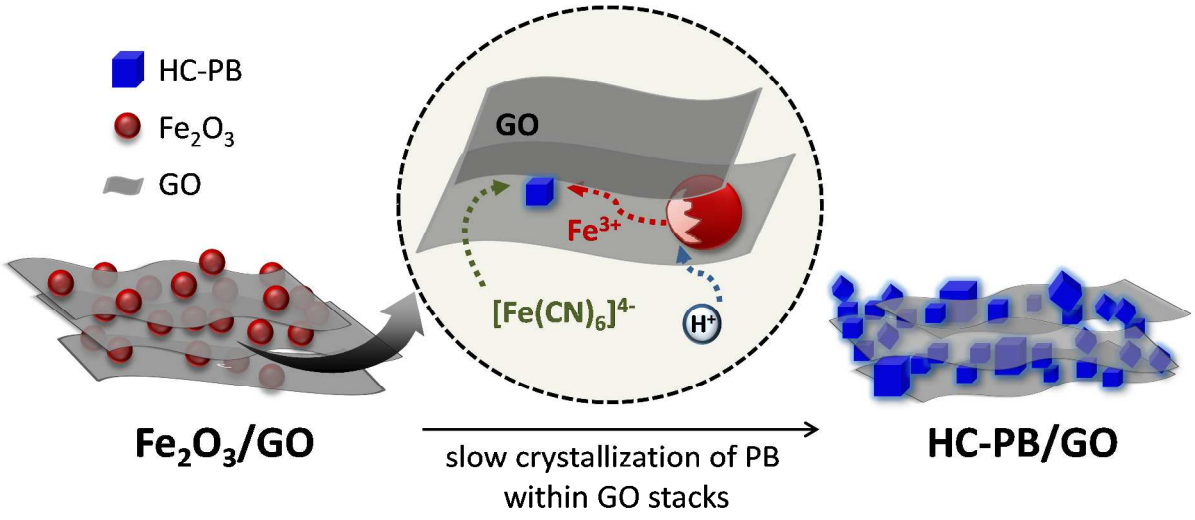

Figure 1

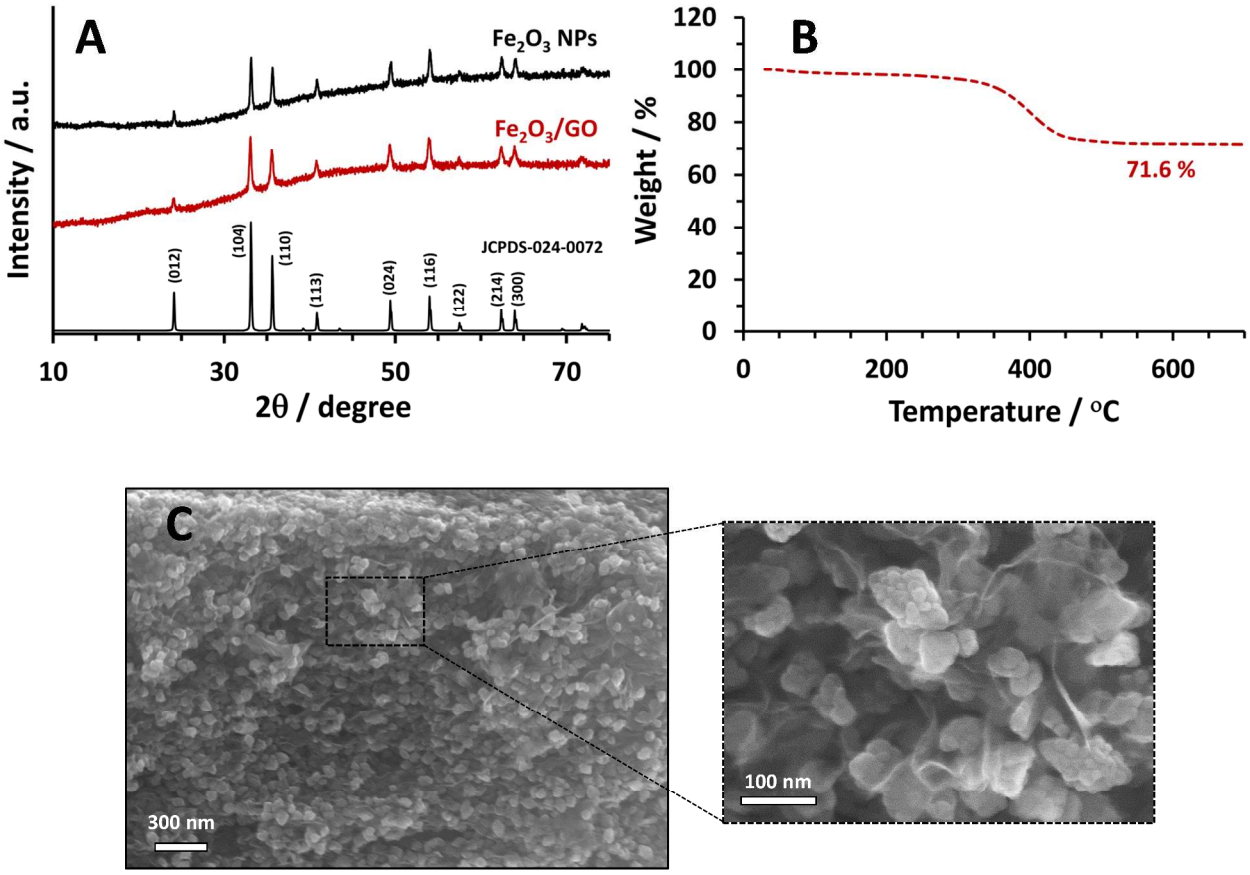

Figure 2

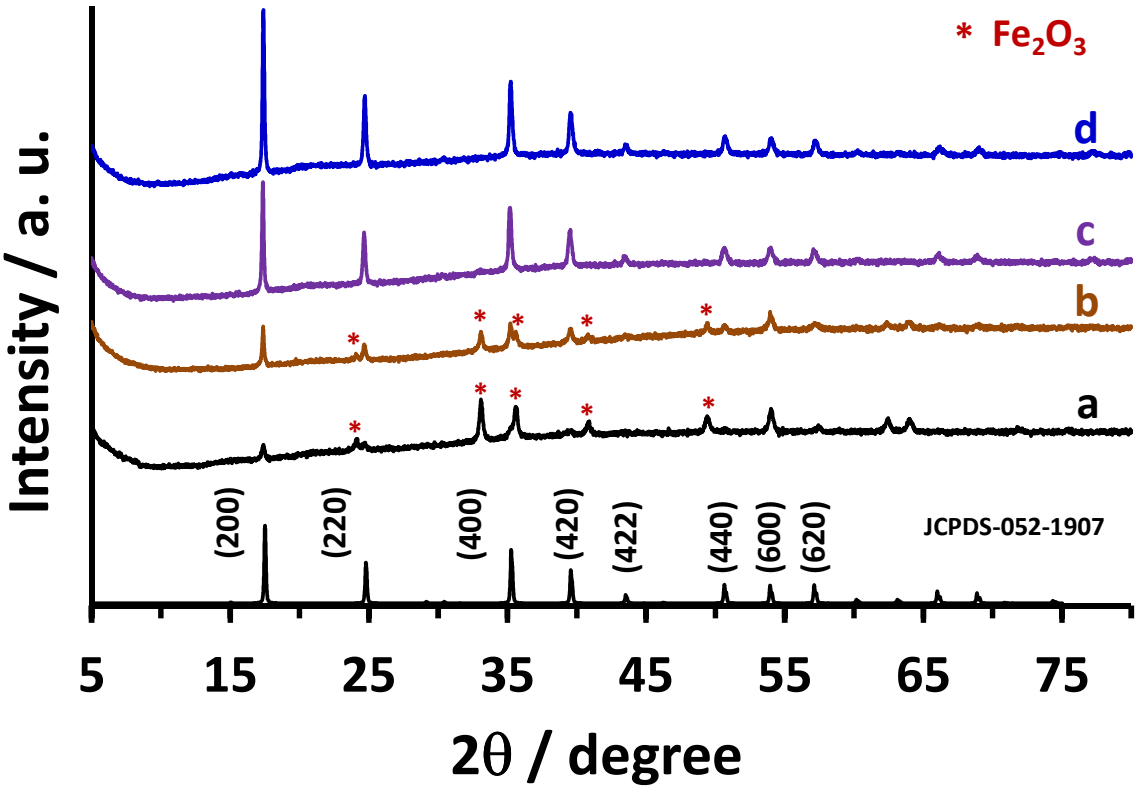

Figure 3

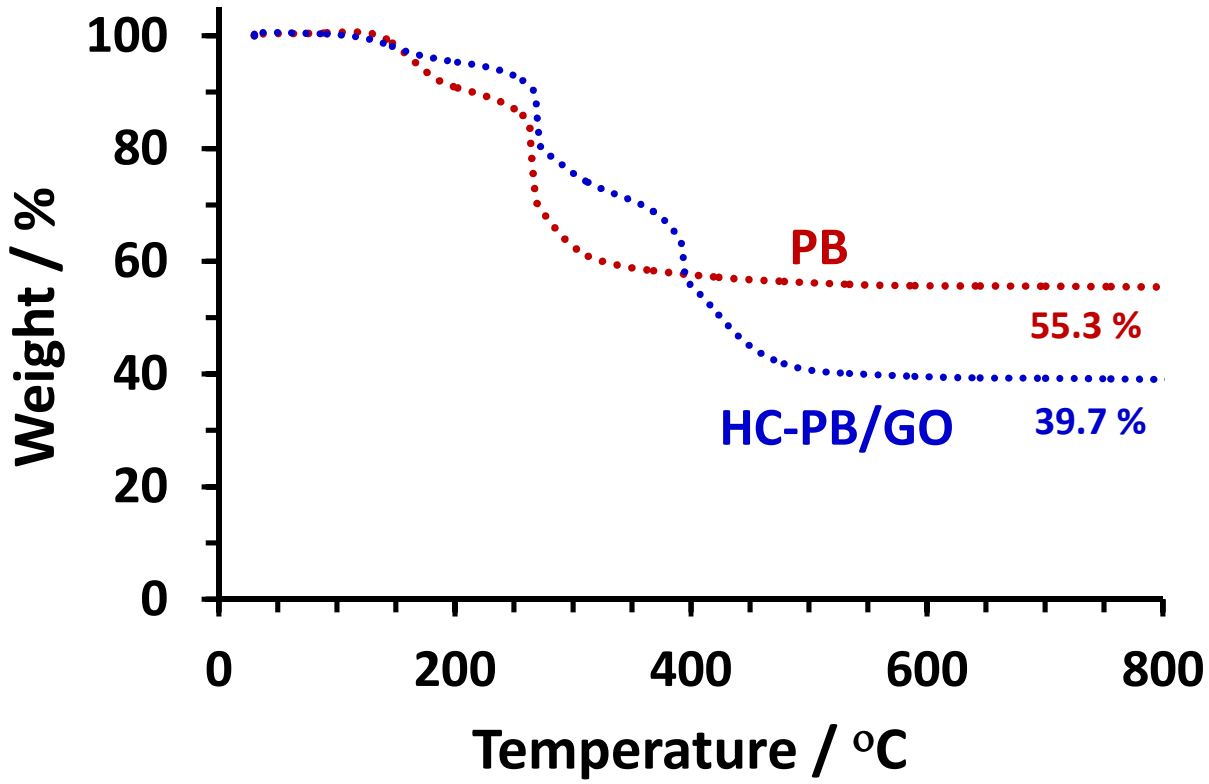

Figure 4

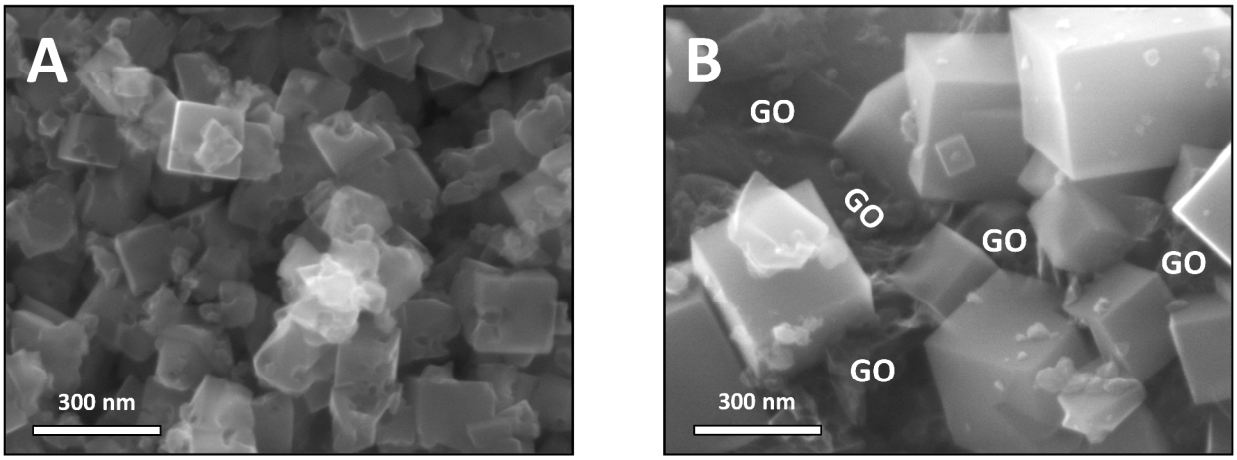

Figure 5

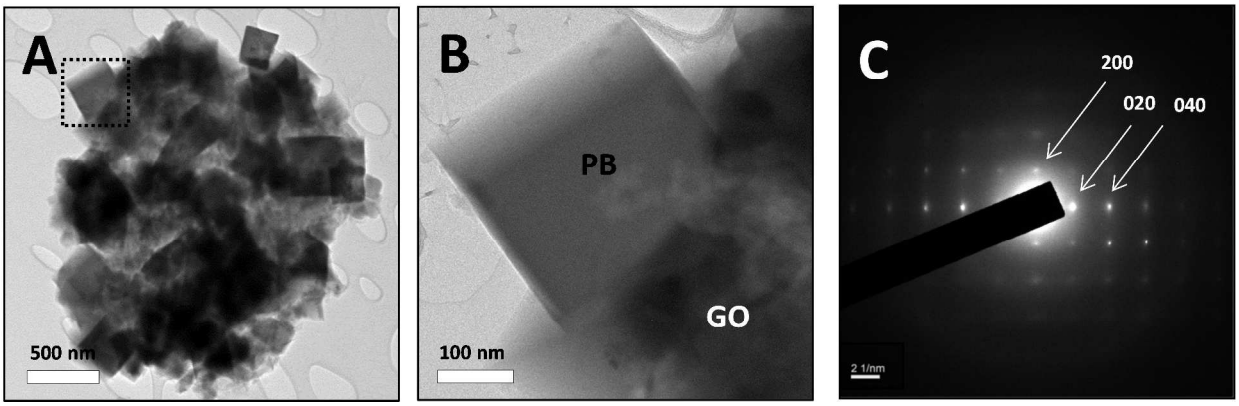

Figure 6

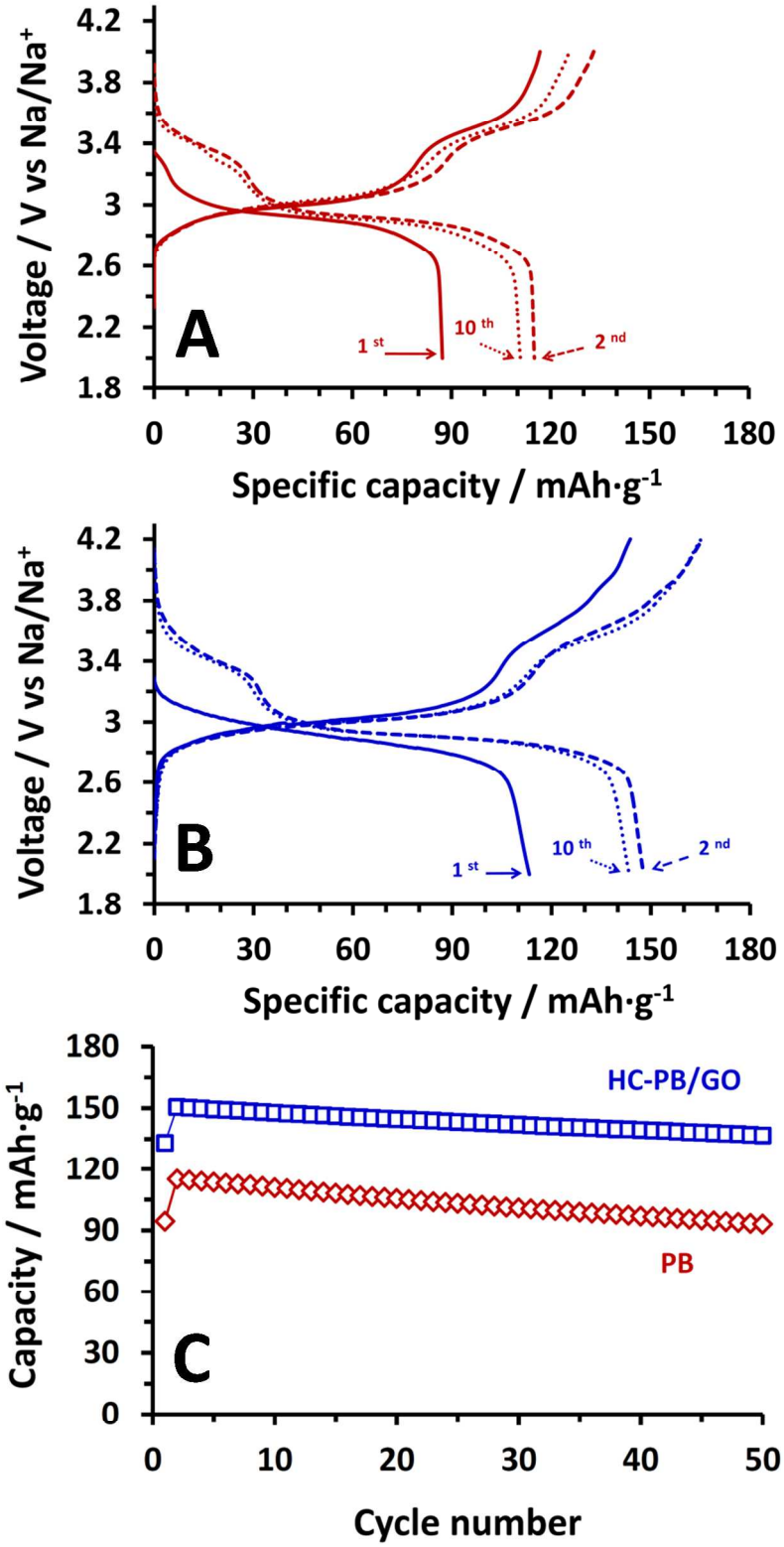

Figure 7

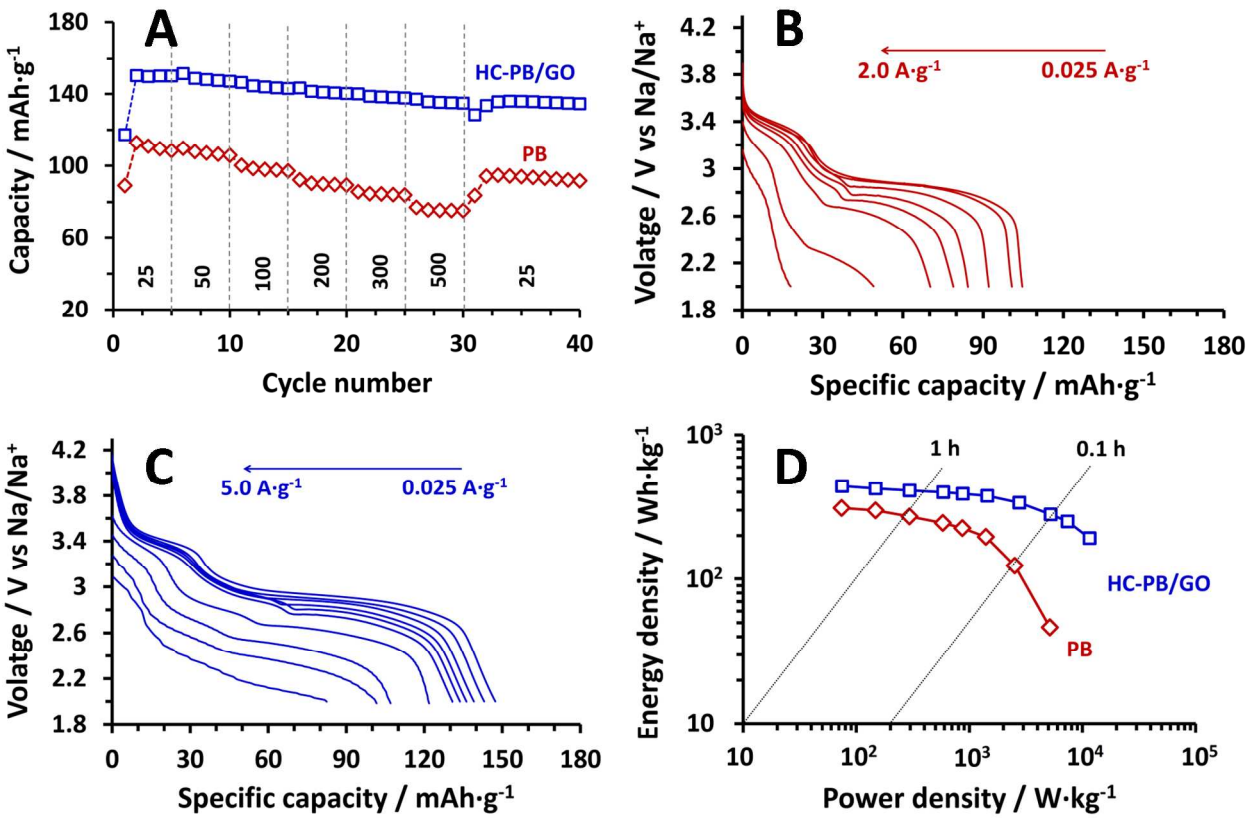

Figure 8

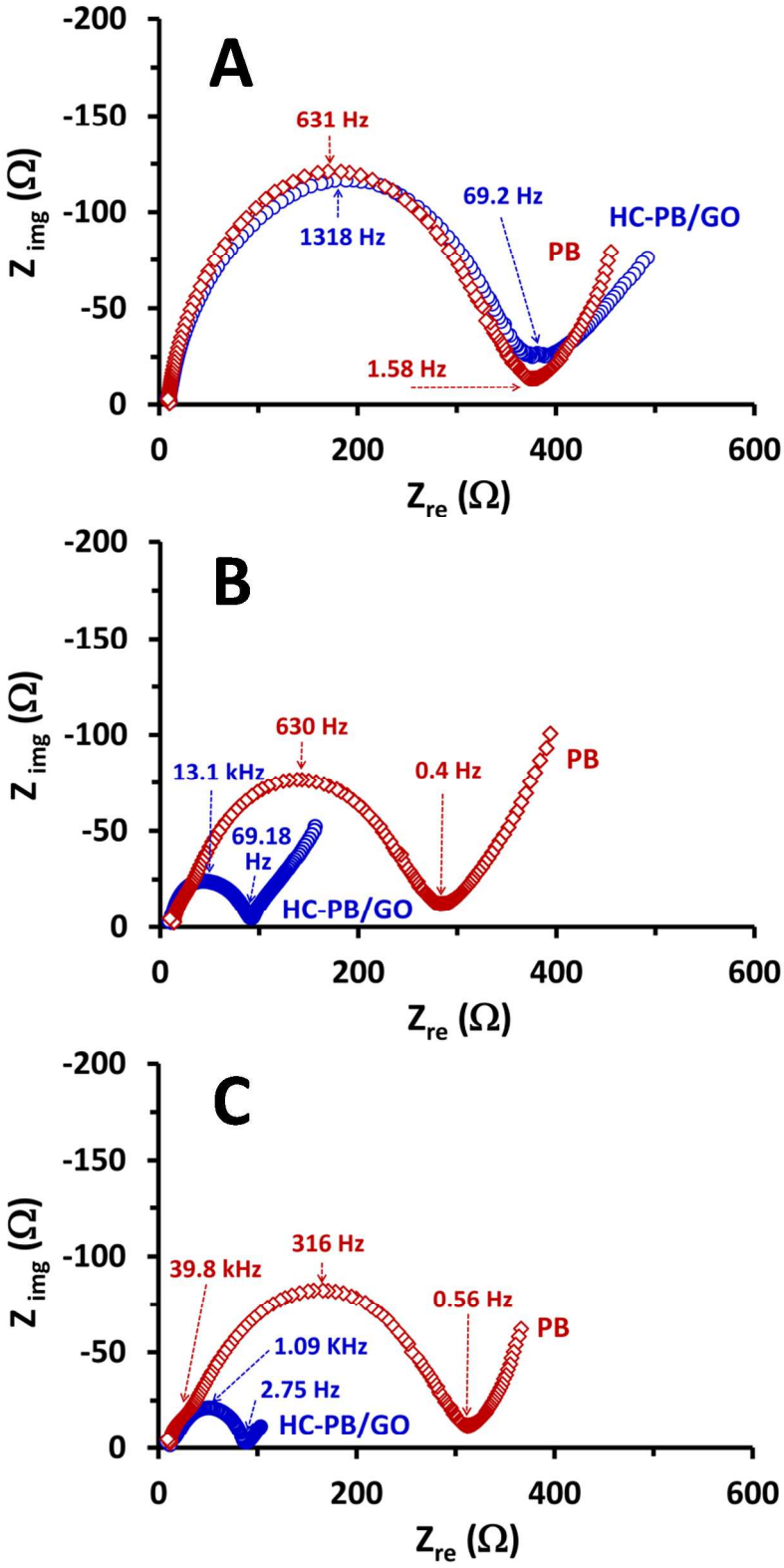

Figure 9

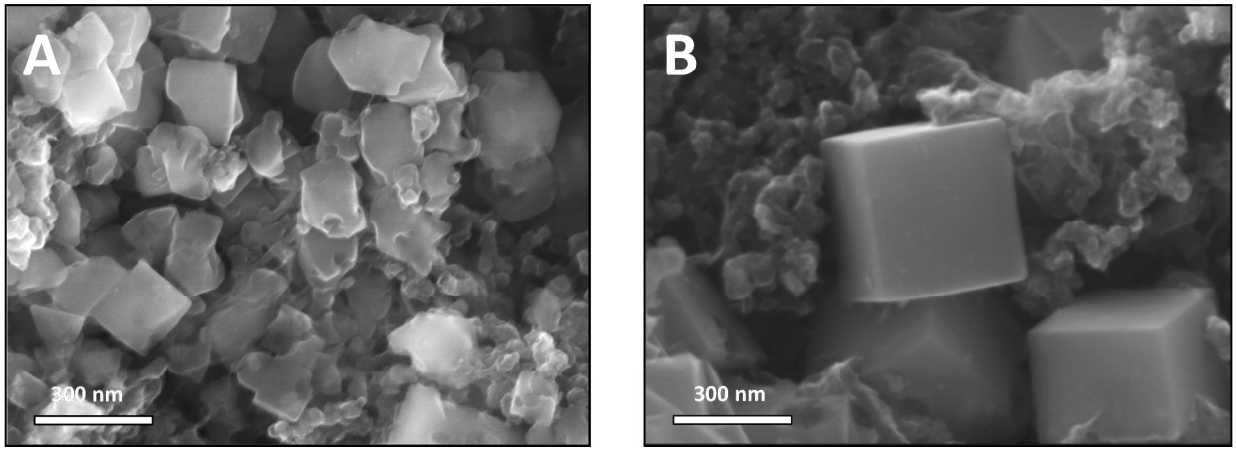

RSC Advances

Table of contents

Slow ion release facilitated synthesis of highly crystalline Prussian Blue/Graphene Oxide composite as a Na ion battery cathode